IEEE Robotics and Automation Letters (RA-L) paper, presented at ICRA 2026, Vienna, Austria. Cite as RA-L paper.

Viscoelasticity-Based Mechanistic Modeling and Control of Bending Pneumatic Muscles

Zishuo Zhao, Baoguo Xu, *Member, IEEE*, Jiajin Wang, *Graduate Student Member, IEEE*, Jianwei Lai, Yifei Wang, Huijun Li, and Aiguo Song, *Senior Member, IEEE*

***Abstract*—Predicting the kinematics of bending pneumatic muscles (BPMs) remains challenging due to the necessity for models that effectively address the pronounced hysteresis and creep inherent in soft materials. While prior research has predominantly focused on phenomenological and data-driven modeling approaches, this study introduces a viscoelasticity-based mechanistic model (VBMM) and a feedforward-feedback hybrid control system tailored for BPMs. First, the VBMM is developed by leveraging the principles of viscoelasticity—a common property of soft materials and a mechanistic driver of hysteresis and creep. Second, we address the computational challenge arising from the history-dependent viscoelastic response of BPMs, where the current state depends on the cumulative stress-strain history. Conventional methods incur escalating computational costs over time, rendering real-time control impractical. To resolve this, we propose a sliding window-based long-term prediction mechanism (long-term VBMM) that maintains model accuracy while significantly reducing computational overhead. Finally, a hybrid control system integrating the long-term VBMM as a feedforward compensator with feedback correction is designed to achieve BPM motion tracking. Experimental validation confirms the VBMM's superior predictive accuracy (error $< 3.69\%$) and demonstrates the control system's effectiveness.**

***Index Terms*—Viscoelasticity, hysteresis, modeling, control, and learning for soft robots, soft sensors and actuators.**

I. Introduction

PNEUMATIC muscles (PMs) exhibit various advantages in human–robot interactions, such as excellent flexibility, high power-to-weight ratios, lightweight materials, holding great potential for applications in grasping [1], flexible robotic arms [2] and medical rehabilitation [3].

However, some inherent characteristics of PMs, e.g., strong hysteresis [4] and creep [5], make it difficult to be modeled accurately. Hysteresis manifests as an inconsistency in motion states corresponding to the same input air pressure during loading and unloading cycles, resulting in characteristic hysteresis loops, as shown in Fig. 1(a). Creep refers to the persistent motion of PMs after pressure stabilization, as shown in Fig. 1(b). It is clear that when the air pressure stops changing after 1 s, the BPM still moves to 2.3 s (yellow curve). These properties lead to a particular challenge for PM modeling.

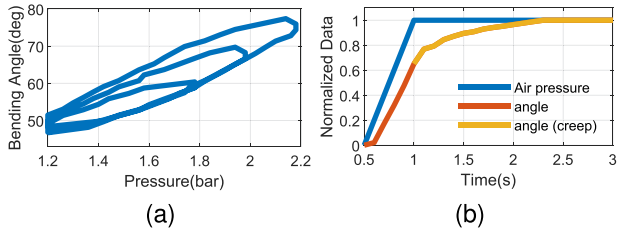

Fig. 1. Hysteresis and creep properties of pneumatic muscles. (a) Hysteresis loop. (b) Creep phenomenon.

Currently, the models of the PMs are categorized into three main types: phenomenological models [6], [7], [8], [9], data-driven models [10], [11], [12], [13] and mechanistic models [14], [15], [16], [17], [18].

The generalized Prandtl-Ishlinskii (GPI) model [8], [9] is the most widely used phenomenological approach, approximating hysteresis via play operators to balance simplicity and accuracy. For example, Zhang [8] employed GPI to linearize a PMs robot system. Other methods include cubic functions [6] and three-element models [7]. While phenomenological models partially explain PMs hysteresis, their accuracy declines under variable pneumatic loading conditions.

With the advancement of learning-based algorithms, data-driven models have become more accurate. For instance, J. Wang [10], [11] improved the Koopman-MPC framework for BPM control, while S. Wang [12] used LSTM networks to capture PMs' historical dependence. However, despite their accuracy, these methods require large training datasets for generalization and lack physical interpretability.

Mechanistic models fall into three categories: Lagrangian dynamics, energy models, and microelement analysis. [16] modeled BPM dynamics using Euler-Lagrange equations, while [1], [15] derived energy models from the work-energy theorem. Microelement analysis involves force, constitutive, and deformation steps—[14], [17] used hyperelastic rubber relations to approximate PMs' nonlinearity, though this fails to explain hysteresis or creep.

Received 26 February 2025; accepted 2 July 2025. Date of publication 23 July 2025; date of current version 31 July 2025. This article was recommended for publication by Associate Editor H. Rodrigue and Editor C. Laschi upon evaluation of the reviewers' comments. This work was supported in part by the National Key Research and Development Program of China under Grant 2022YFC2405602, in part by the Natural Science Foundation of Jiangsu Province under Grant BK20221464, and in part by the National Natural Science Foundation of China under Grant 92148205. *(Corresponding author: Baoguo Xu.)*

The authors are with the State Key Laboratory of Digital Medical Engineering, Jiangsu Key Laboratory of Robot Perception and Control, School of Instrument Science and Engineering, Southeast University, Nanjing 210096, China (e-mail: zhaozishuo@seu.edu.cn; xubaoguo@seu.edu.cn; wangjiajin@seu.edu.cn; 101300484@seu.edu.cn; 230219243@seu.edu.cn; lihuijun@seu.edu.cn; a.g.song@seu.edu.cn).

Digital Object Identifier 10.1109/LRA.2025.3592102

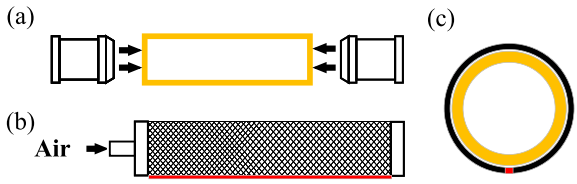

Fig. 2. Fabrication process of the BPM. (a) Two plugs are stuffed into both ends of the elastic tube. (b) A pneumatic quick coupler is installed and one generatrix of the braided mesh tube is sewn. (c) The cross section of the BPM.

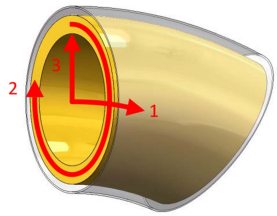

Fig. 3. Coordinate system of the BPM. The axial, circumferential, and radial directions of the BPM are defined as directions 1, 2, and 3.

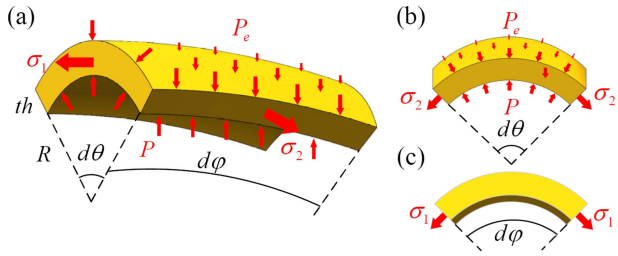

Fig. 4. Microelement force analysis of the BPM. (a) The isometric view of the microelement. (b) The front view. (c) The side view.

To address these critical limitations, we propose a novel viscoelasticity-based mechanistic model (VBMM) for BPMs. Viscoelasticity [19] is a property common to soft polymeric materials. Viscoelastic constitutive models typically exhibit history dependence and are generally more computationally intensive than hyperelastic models. Within moderate deformation ranges, the generalized Maxwell model [20] remains the most widely used linear viscoelastic approach based on the Boltzmann superposition principle. For large deformations, Reese [21] proposed a nonlinear framework using thermodynamic laws and multiplicative decomposition. Bergström [22] introduced a model separating stress into equilibrium and rate-dependent parts. Bagley [23] later linked molecular theories of viscoelastic fluids to fractional calculus.

The essence of viscoelasticity lies in energy dissipation during deformation, causing strain to lag behind stress—meaning deformation lags behind external load changes. This is a key cause of hysteresis and creep in BPMs [24]. To address this, we analyze BPM microelement forces in bending and derive a high-precision model using viscoelastic constitutive relations. However, the VBMM's computational cost grows over time. To reduce this burden and enable long-term predictions, we optimize the VBMM with a sliding window mechanism (long-term VBMM). Finally, we design a feedforward-feedback hybrid control system, using the long-term VBMM as the feedforward, achieving high control performance. The contributions of this work are summarized as follows,

- A viscoelasticity-based mechanistic model to model the hysteresis and creep of the BPM with high accuracy (error $< 3.69\%$).
- A long-term model prediction mechanism based on a sliding window to reduce the computational time of the VBMM (97% reduction).
- A feedforward-feedback hybrid control system using the long-term VBMM as the feedforward, which can effectively control the BPM's bending motion.

II. Viscoelasticity-Based Mechanistic Modeling

The fabrication process of the BPM is illustrated in Fig. 2. Firstly, two plugs (3D printed) are stuffed into both ends of the silicone rubber elastic tube (Fig. 2(a)). Elastic components are color-coded yellow in subsequent figures for clarity. The elastic tube is then covered with a braided mesh tube and tightened with metal cable ties at both ends. A pneumatic quick coupler is installed at one end of the plug for connecting to an air compressor, as shown in Fig. 2(b). Finally, one generatrix of the braided mesh tube is sewn with a non-stretchable thread (red line in Fig. 2(b)). Upon pressurization, differential expansion occurs: while the elastic tube undergoes axial elongation, the constrained suture side restricts symmetric expansion, inducing controlled bending deformation. Fig. 2(c) presents the cross-sectional configuration, demonstrating the composite structure's layered composition.

The deformation mode of BPMs depends on their initial helix angle α_0: $\alpha_0 < 36.25^\circ$ yields radial contraction and axial elongation, while $\alpha_0 > 36.25^\circ$ produces radial expansion and axial shortening [1], [25]. This study specifically focuses on the elongating BPMs.

The coordinate system is set up in Fig. 3, with BPM axial direction as direction 1, circumferential direction as direction 2, and radial direction as direction 3. The grey transparent part in Fig. 3 is the braided mesh tube.

A. Microelement Force Analysis of the BPM

Microelement force analysis of the BPM's elastic tube [26] is shown in Fig. 4. The microelement is subjected to axial stresses σ_1 on both axial sides and circumferential stresses σ_2 on both circumferential sides. The element experiences internal air pressure P and externally applied linear pressure P_e from the braided mesh tube constraint. Since the radial deformation is much smaller than the circumferential and axial deformation, the radial stresses are neglected and the wall thickness th of the elastic tube is considered to be fixed. The motion of the BPM can be considered as a quasi-static process. Gravity is neglected because the BPM's mass is very light. Force equilibrium analysis in the radial direction yields:

$$\begin{aligned}&(P - P_e)\, d\theta \cdot R \cdot d\varphi \cdot R_{bend} \\ &= 2\sin\frac{d\theta}{2} \cdot \sigma_2 \cdot th \cdot d\varphi \cdot R_{bend} + 2\sin\frac{d\varphi}{2} \cdot \sigma_1 \cdot th \cdot d\theta \cdot R,\end{aligned} \tag{1}$$

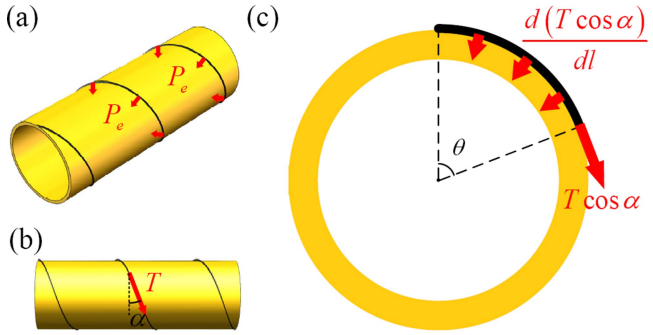

Fig. 5. Schematic diagram of the linear pressure P_e exerted by the braided mesh tube on the elastic tube. (a) The isometric view. (b) The side view. (c) The cross section.

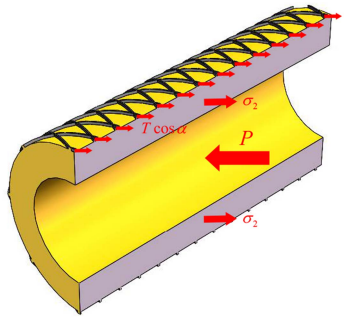

Fig. 6. Schematic diagram of air pressure equilibrium. The air pressure P, circumferential stress σ_2 and thread tension $T\cos\alpha$ are balanced normal to the longitudinal section.

where R_{bend} denotes the bending radius of the whole BPM, R denotes the inner radius, $d\theta$ and $d\varphi$ correspond to the microelement bending angles in circumferential and axial directions. The simplification leads to:

$$\frac{P-P_e}{th}-\frac{\sigma_2}{R}-\frac{\sigma_1}{R_{bend}}=0. \tag{2}$$

Braided mesh tubes consist of multiple strands of threads twisted in a spiral pattern. The pressure P_e exerted by the braided mesh tube on the elastic tube, as shown in Fig. 5(a), can be derived from the linear pressure $\frac{dT}{dl}$ exerted by a single thread on the elastic tube, where T represents the thread tension. The helix angle of the thread is denoted as α (Fig. 5(b)). The circumferential component of T is $T\cos\alpha$, and the linear pressure can thus be denoted as $\frac{d(T\cos\alpha)}{dl}$. Fig. 5(c) shows the cross section of the BPM. A section of arc with radian θ is taken for analysis. By balancing the vertical components of the thread-induced pressure and the tension, it can be obtained:

$$\int_0^{\theta}\frac{d\left(T\cos\alpha\right)}{dl}\frac{Rd\theta'}{\cos\alpha}\cos\theta'=T\cos\alpha\sin\theta. \tag{3}$$

The simplification leads to:

$$P_e=\frac{d\left(T\cos\alpha\right)}{dl}=\frac{T}{R}\cos^2\alpha. \tag{4}$$

B. Viscoelastic Constitutive Relation

The constitutive relation describes the relationship between stress σ and strain ε, expressed as $\sigma=f(\varepsilon)$. Previous studies have predominantly employed hyperelastic constitutive relations [14], [17]. However, these approaches predict identical material responses during pneumatic loading and unloading, failing to capture the hysteresis behavior intrinsic to BPMs. The difference between the viscoelastic constitutive relation and the hyperelastic constitutive relation is that the shear modulus G and the bulk modulus K are no longer fixed but vary with time, i.e., $\sigma=f(\varepsilon,t)$, which causes hysteresis and creep. According to the Boltzmann superposition principle, the linear viscoelastic constitutive relation at varying air pressure is:

$$\begin{aligned}\sigma_{ij}(t)=&2G_\infty\varepsilon_{ij}\left(t_0\right)+\delta_{ij}\left(K_\infty-\frac{2}{3}G_\infty\right)\varepsilon_{kk}\left(t_0\right)\\&+2\sum_{t_i=t_1}^{t}G\left(t-t_i\right)\nabla\varepsilon_{ij}\left(t_i\right)\\&+\delta_{ij}\sum_{t_i=t_1}^{t}\left[K\left(t-t_i\right)-\frac{2}{3}G\left(t-t_i\right)\right]\nabla\varepsilon_{kk}\left(t_i\right),\end{aligned} \tag{5}$$

where ∇ denotes the backward difference operator, i.e., $\nabla\varepsilon_{ij}(t_i)=\varepsilon_{ij}(t_i)-\varepsilon_{ij}(t_{i-1})$, G_∞, K_∞ denote the shear modulus and bulk modulus as time t tends to infinity. $G(t)$ and $K(t)$ are represented by the generalized Maxwell models [20]:

$$\begin{aligned}G(t)&=G_\infty+G_1\exp\left(-\frac{t}{\tau_G}\right)\\K(t)&=K_\infty+K_1\exp\left(-\frac{t}{\tau_K}\right),\end{aligned} \tag{6}$$

where G_∞, G_1, τ_G, K_∞, K_1 and τ_K represent the parameters to be optimized. The rationale for using a linear viscoelastic constitutive model will be demonstrated in the experimental section.

C. Air Pressure Equilibrium

The air pressure P, circumferential stress σ_2 and the circumferential component of thread tension $T\cos\alpha$ are balanced normal to the longitudinal section, as illustrated in Fig. 6. This equilibrium is described by the following air pressure equilibrium equations:

$$\sigma_2^{\theta=0}th\cdot l_0+\sigma_2^{\theta=\pi}th\cdot l_{\theta=\pi}+T\cos\alpha=P\cdot 2R\cdot l_{\theta=\pi/2}, \tag{7}$$

where $\sigma_2^{\theta=0}$, $\sigma_2^{\theta=\pi}$ denote the circumferential stresses at circumferential angles of 0° and 180°, and l_0, $l_{\theta=\pi}$ and $l_{\theta=\pi/2}$ denote the lengths at circumferential angles of 0°, 180° and 90°.

D. Geometric Deformation Analysis

Fig. 7 illustrates the cross section of the BPM, demonstrating its radial expansion under decreasing air pressure (indicated by color transition from transparent light yellow to deep yellow). Assuming that the cross section of the BPM maintains a circular shape after deformation, the centre of the circle before

Fig. 7. Schematic diagram of the relationship between radial displacement u_3 and circumferential strain ε_2.

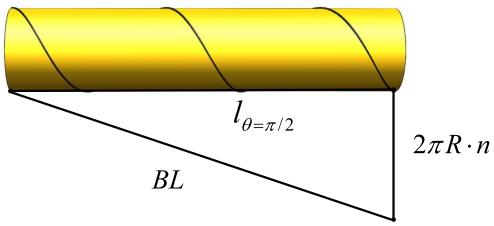

Fig. 8. Schematic diagram of the relationship between radial displacement u_3 and axial strain ε_1.

deformation is denoted as O_0 and the radius as R_0. The centre of the circle after deformation is denoted as O and the mean radius as R. The radial displacement of a microelement at a circumferential angle of 180° is denoted as $u_3^{\theta=\pi}$, as shown in Fig. 7(a). The mean radius R after deformation can be calculated in terms of the radial displacement $u_3^{\theta=\pi}$:

$$R = R_0 + \frac{1}{2}u_3^{\theta=\pi}. \tag{8}$$

Taking a section of arc microelement for analysis, as shown in Fig. 7(b), the circumferential strain ε_2 can be expressed as:

$$\lambda_2 = 1 + \varepsilon_2 = \frac{l'_{arc}}{l_{arc}}, \tag{9}$$

where λ_2 denotes the circumferential stretch ratio, l_{arc} and l'_{arc} denote the arc length before and after the deformation. Assuming that the radian of the arc microelement is constant, the circumferential strain ε_2 can be expressed as:

$$\varepsilon_2 = \frac{l'_{arc}}{l_{arc}} - 1 = \frac{R'}{R_0} - 1 = \frac{u_3}{R_0}, \tag{10}$$

where R' denotes the corresponding radius of the arc microelement.

Compared to the elastic tube, the deformation of the braided mesh tube is negligible. Therefore, the length of the thread is fixed, denoted by BL, as illustrated in Fig. 8. During the bending of the BPM, although the length l and the inner radius R continuously vary, the thread length BL remains unchanged, then there is:

$$\begin{aligned} BL^2 &= {l_{\theta=\pi/2}}^2 + (2\pi R \cdot n)^2 \\ &= \left(\lambda_1^{\theta=\pi/2} l_0\right)^2 + (2\pi R \cdot n)^2, \end{aligned} \tag{11}$$

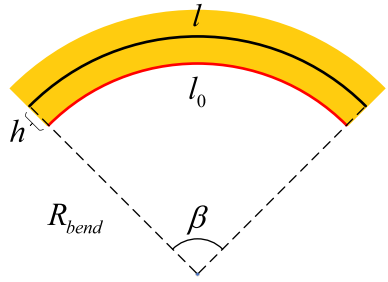

Fig. 9. Side view of the BPM when bending. Red line represents the non-stretchable suture.

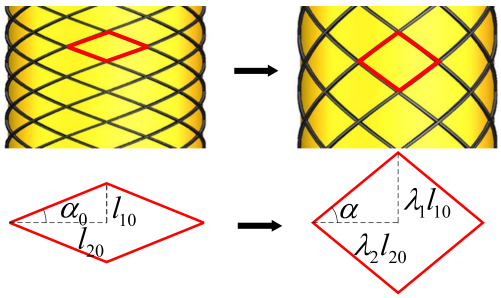

Fig. 10. Changes in the mesh of the braided mesh tube during BPM bending.

where n denotes the number of turns the thread wraps around the elastic tube. Combined with (8), this gives:

$$\varepsilon_1^{\theta=\pi/2} = \frac{1}{l_0}\sqrt{BL^2 - 4\pi^2 n^2\left(R_0 + \frac{1}{2}u_3^{\theta=\pi}\right)^2} - 1. \tag{12}$$

Fig. 9 shows a side view of the BPM in bending. A non-stretchable suture (red line) along one generatrix is defined as the neutral layer with invariant length l_0. The axial strain ε_1 in the offset generatrix (black line) positioned at vertical distance h from this neutral layer can be derived through length variation analysis. Given the initial length l_0 and deformed length l, the strain formulation becomes:

$$\varepsilon_1 = \frac{l - l_0}{l_0} = \frac{(R_{bend} + h)\,\beta - R_{bend}\beta}{R_{bend}\beta} = \frac{h}{R_{bend}}, \tag{13}$$

where β denotes the bending angle of the BPM. Under constant bending angle β, the axial strain ε_1 depends solely on the vertical distance h to the neutral layer. Equation (14) establishes the linear proportionality between ε_1 and h, yielding $\varepsilon_1^{\theta=\pi} = 2\varepsilon_1^{\theta=\pi/2}$. The bending angle β can be expressed by the radial displacement $u_3^{\theta=\pi}$ of the microelement at $h = 2R$:

$$\beta = \frac{l_0}{R_{bend}} = \frac{l}{2R + R_{bend}} = \frac{\lambda_1^{\theta=\pi} l_0}{R_{bend} + 2R_0 + u_3^{\theta=\pi}}. \tag{14}$$

The simplification leads to:

$$\beta = \frac{\varepsilon_1^{\theta=\pi} l_0}{u_3^{\theta=\pi} + 2R_0}. \tag{15}$$

It is assumed that the mesh of the braided mesh tube always maintains a rhombic structure, as shown in Fig. 10. Since the thread length remains constant, the side length of the rhombus

also remains constant during the bending of the BPM. The initial helix angle of the thread is denoted as α_0 and the helix angle after elongation as α. Then there is:

$$\frac{l_{20}}{\cos\alpha_0} = \frac{\lambda_2 l_{20}}{\cos\alpha}. \tag{16}$$

The simplification leads to:

$$\cos\alpha = \cos\alpha_0\left(1+\varepsilon_2\right). \tag{17}$$

By combining equations (2), (4), (5)–(8), (10), (12), (15) and (17), we derive the inverse VBMM $P(\beta)$ as:

$$\begin{cases} u_3 = -2R_0 + \frac{2\sqrt{\overline{D}\beta^2+\overline{E}}-2l_0\beta}{\beta^2+4\pi^2n^2} \\ P = \frac{th}{R_0+0.5u_3}\left(\sigma_2 + \frac{\sigma_2\overline{G}(u_3)+\sigma_1\left(\overline{F}(u_3)-1\right)}{1-2\overline{G}(u_3)\overline{F}(u_3)}\right) \end{cases}, \tag{18}$$

where $\overline{D} = {l_0}^2 + 4\pi^2n^2{R_0}^2$, $\overline{E} = 16\pi^4n^4{R_0}^2$, $\overline{G}(u_3) = l_0\cos\alpha_0(1+u_3/R_0)$, $\overline{F}(u_3) = \sqrt{\overline{A}{u_3}^2+\overline{B}u_3+1}$, $\overline{A} = -\pi^2n^2/{l_0}^2$, $\overline{B} = -4\pi^2n^2R_0/{l_0}^2$, $\sigma_1 = f_1(\boldsymbol{u_3}, t)$, $\sigma_2 = f_2(\boldsymbol{u_3}, t)$, $\boldsymbol{u_3} = \{u_3^{t_0}, u_3^{t_1}, \ldots, u_3^{t}\}$. The forward VBMM $\beta(P)$ is resolved through numerical methods.

III. Long-Term Model Prediction Mechanism Based on a Sliding Window

The viscoelastic response of BPMs is history-dependent under the Boltzmann superposition principle, where current states depend on complete stress-strain histories. As evident from (5), this formulation incurs linearly growing computational costs with time evolution, fundamentally limiting long-term predictions and real-time control. To reduce the computational burden, this section proposes a long-term model prediction mechanism based on a sliding window (simplified as long-term VBMM).

Equation (6) reveals that both the shear modulus G and the bulk modulus K exhibit time-dependent decay governed by negative exponential functions of time t. When t is sufficiently large, the shear modulus G and bulk modulus K tend to constant values. In other words, the shear modulus G and bulk modulus K corresponding to the initial moment t_0 and the truncation moment t_s ($t_s < t$) are nearly the same. Therefore, when calculating the stress at the current moment t, a sliding window can be set up so that only the strains within the window duration T_{win} ($T_{win} = t - t_s$) are involved in the iterative calculation, as illustrated in Fig. 11. Equation (5) is improved as:

$$\begin{aligned} \sigma_{ij}(t) = {} & 2G_\infty\varepsilon_{ij}(t_0) + \delta_{ij}\left(K_\infty - \frac{2}{3}G_\infty\right)\varepsilon_{kk}(t_0) \\ & + 2\sum_{t_i=t_{s+1}}^{t} G(t-t_i)\nabla\varepsilon_{ij}(t_i) \\ & + \delta_{ij}\sum_{t_i=t_{s+1}}^{t}\left[K(t-t_i) - \frac{2}{3}G(t-t_i)\right]\nabla\varepsilon_{kk}(t_i) \\ & + 2G(t_s)\left[\varepsilon_{ij}(t_s) - \varepsilon_{ij}(t_0)\right] \\ & + \delta_{ij}\left[K(t_s) - \frac{2}{3}G(t_s)\right]\left[\varepsilon_{kk}(t_s) - \varepsilon_{kk}(t_0)\right]. \end{aligned} \tag{19}$$

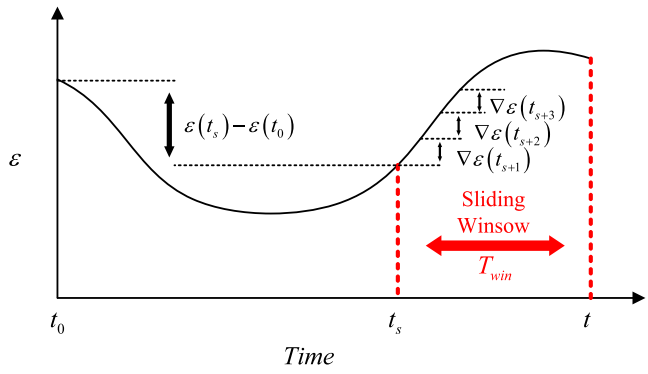

Fig. 11. Schematic diagram of long-term model prediction mechanism based on a sliding window. Only the strains within the window duration T_{win} are involved in the iterative calculation.

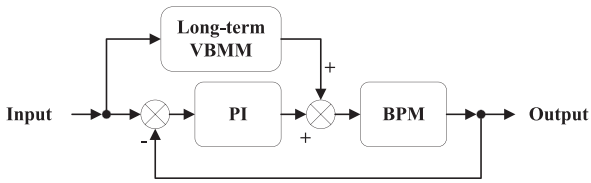

Fig. 12. Control block diagram of the feedforward-feedback hybrid control system with the long-term VBMM as the feedforward.

IV. Feedforward-Feedback Hybrid Control System

The long-term VBMM is used as the feedforward and combined with a PI controller to form a feedforward-feedback hybrid control system (simplified as VBMM-PI), which is more suitable for real-time control than the VBMM. The control block diagram is shown in Fig. 18. The mathematical expression for the VBMM-PI controller is:

$$P_{out}(k+1) = P\left(\beta_{in}(k)\right) + \mathrm{P}\cdot e(k) + \mathrm{I}\cdot\sum_{0}^{k} e(k), \tag{20}$$

where $e(k)$ and $\beta_{in}(k)$ represent the feedback error and the expected bending angle at step k, $P_{out}(k+1)$ represents the output air pressure at step $k+1$ and $P(\cdot)$ represents the inverse of the long-term VBMM ((18)). P and I denote adjustable parameters of the PI controller.

V. Experimental Results

This section describes the BPM experimental platform and a series of experiments used to verify the precision of the viscoelasticity-based mechanistic model and the validity of the feedforward-feedback hybrid control system.

A. System Overview

The BPM system is shown in Fig. 13. The inlet port of the proportional valve (Festo VPPE-3-1, Germany) connects to the air compressor, and the outlet port connects to the BPM. The flex sensor (Bendlabs, USA) detects the bending angle and feeds back to Simulink Desktop Real-Time, where the model prediction and control algorithm are executed. Simulink

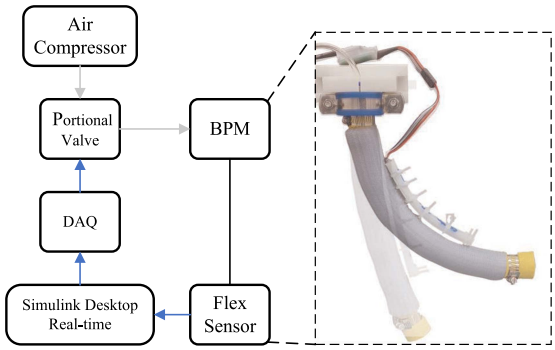

Fig. 13. System connection diagram. Grey arrows represent airflow pathways. Blue arrows represent electricity pathways. The solid black line represents physical connections.

TABLE I
GEOMETRY PROPERTY PARAMETERS OF THE BPM

Parameters	Value
Wall thickness th	2(mm)
Initial helix angle α_0	30(°)
Initial radius R_0	16.73(mm)
Initial length l_0	195.9(mm)
Number of wrapping turns n	7.43
Thread length BL	804.1(mm)

Desktop Real-Time generates analog voltage signals via a data acquisition card (DAQ, Advantech PCIe-1824, China) to control the proportional valve, thus regulating the internal air pressure of the BPM. System sampling frequency and control frequency are both 10 Hz.

The BPM's geometric parameters are listed in Table I. Uniaxial tensile stress relaxation tests were conducted on an Instron-685 C machine at loading rates of 300 and 400 mm/min, matching pneumatic muscle operational strain rates. Specimens were stretched to 15–40% strain (covering the working range of 15–30%), with each strain level held constant for 1 min. Since significant changes only occur within the first 10 s, we only present the initial 10 s curve (Fig. 14). The material exhibited significant stress decay during holding, confirming viscoelasticity. The derived relaxation modulus (Fig. 14(c)) shows nearly overlapping curves across all tested strains and rates (Mean Standard Deviation: 0.00179 MPa, Mean Coefficient of Variation: 6.53%), adhering to the Boltzmann superposition principle. This consistency justifies the adoption of a linear viscoelastic model for strains within 15–40%.

We employed $E(t) = E_\infty + E_1 e^{-t/\tau_1}$ to fit the relaxation modulus curves, where E_∞, E_1 and τ_1 represent the material property parameters to be determined. Using nonlinear least-squares optimization with the experimental data shown in Fig. 14(c), we obtained $E_\infty = 0.0272 \times 10^6$, $E_1 = 0.0549 \times 10^6$ and $\tau_1 = 0.399$ (Fig. 14(d)). Error analysis yielded the following metrics: RMSE = 0.00192MPa, $R^2 = 0.873$, and MAPE = 5.472%. The fitting errors confirm the linear viscoelastic model's accuracy in characterizing the material behavior. As silicone rubber is an incompressible material, its Poisson's ratio approaches 0.5. The parameters $G_\infty = 0.00905 \times 10^6$, $G_1 = 0.0183 \times 10^6$, $K_\infty = 6.753 \times 10^6$, $K_1 = 13.639 \times 10^6$ and $\tau_G = \tau_K = \tau_1 = 0.399$ required for (6) can be calculated from E_∞, E_1 and τ_1. Specimens were sectioned from commercial tubes, possibly introducing residual stresses that could affect experimental accuracy to some extent. To address this, we used stress relaxation test parameters as initial values and fitted motion data via the VBMM. The BPM was cyclically pressurized (1.2–1.6 bar, ± 0.2 bar/s), while time t, pressure P and bending angle β were recorded. Nonlinear least-squares optimization yielded the material parameters: $G_\infty = 0.00905 \times 10^6$, $G_1 = 0.0183 \times 10^6$, $K_\infty = 6.434 \times 10^6$, $K_1 = 13.645 \times 10^6$ and $\tau_G = \tau_K = \tau_1 = 0.213$.

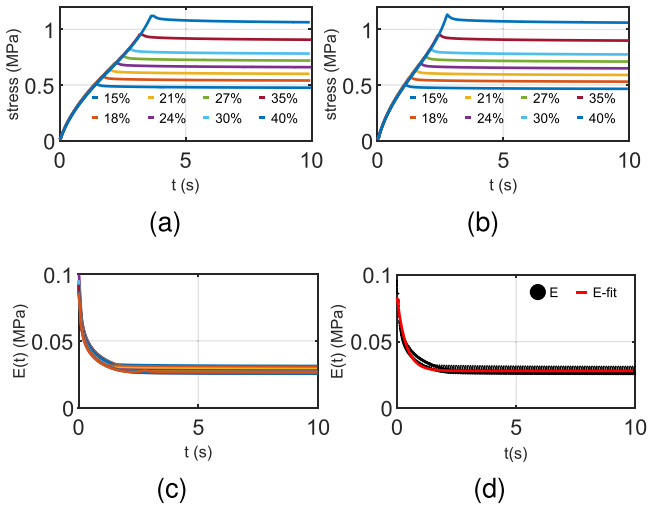

Fig. 14. Results of uniaxial tensile stress relaxation test. (a) 300 mm/min. (b) 400 mm/min. (c) Relaxation modulus curves for all tests. (d) Fitting results.

The window duration T_{win} is set to 20 s through empirical analysis, based on the observed convergence of $G(t)$ and $K(t)$ beyond this temporal threshold (t > 20 s). This configuration achieves computational efficiency while preserving model accuracy.

B. Experiment 1: Viscoelasticity-Based Mechanistic Model Prediction

Two experiments validate the VBMM. First, with fixed loading rate (± 0.2 bar/s), three pressure cycles were performed: 1.2-1.8, 1.2-2.0, and 1.2-2.2 bar (Fig. 15). Second, with fixed pressure range (1.2-2.0 bar), three loading rates were tested: ± 0.114, ± 0.16, and ± 0.267 bar/s (Fig. 16). Five replicates were collected for each case. VBMM predictions used material parameters from relaxation tests (VBMM-mat.) and fitted parameters (VBMM-fit). Blue lines in Fig. 15(b) and Fig. 16(a) show experimental means, with transparent bands indicating standard deviations.

The VBMM-fit demonstrated high precision in variable amplitude tests (Fig. 15), accurately capturing hysteresis and creep dynamics (RMSE=2.122°, MAPE=3.339%, R^2=0.936). It maintained robustness in variable loading rate tests (RMSE=2.137°, MAPE=3.686%, R^2=0.928; Fig. 16).

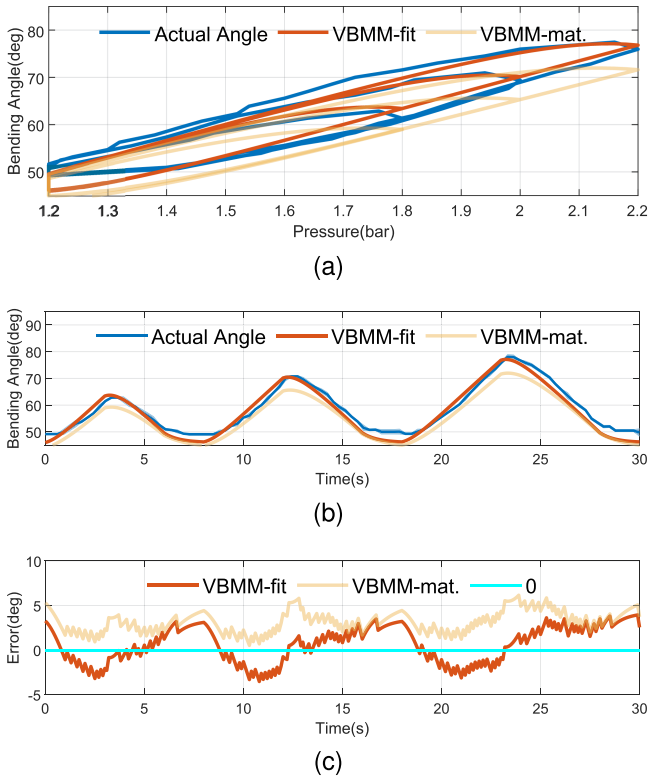

Fig. 15. Results of the variable amplitude experiment (1.8, 2 and 2.2 bar). (a) Pressure-angle graph. (b) Time-angle graph. (c) Time-error graph.

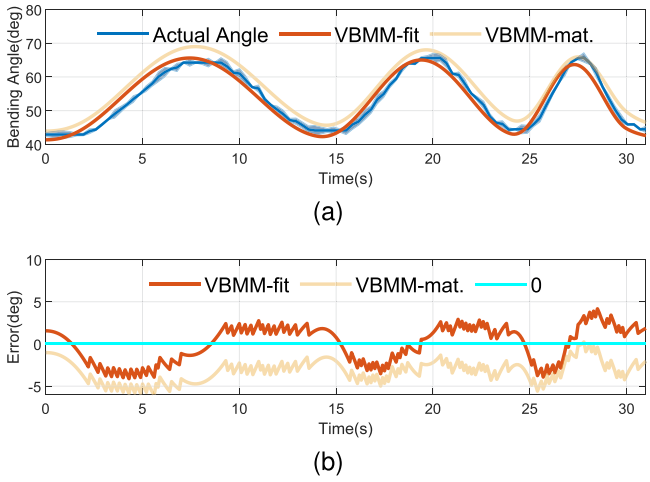

Fig. 16. Results of the variable loading rate experiment ($\pm$ 0.114, $\pm$ 0.16, and $\pm$ 0.267 bar/s). (a) Time-angle graph. (b) Time-error graph.

The VBMM-mat. showed slightly lower accuracy (amplitude tests: RMSE=3.388°, MAPE=5.459%, R^2=0.836; rate tests: RMSE=3.416°, MAPE=6.021%, R^2=0.815) but retained reasonable predictive capability (Figs. 15(b) and 16(a)).

Collectively, these results confirm the VBMM's ability to simultaneously characterize both amplitude-dependent hysteresis and rate-dependent creep phenomena with less than 3.69% MAPE across operational extremes.

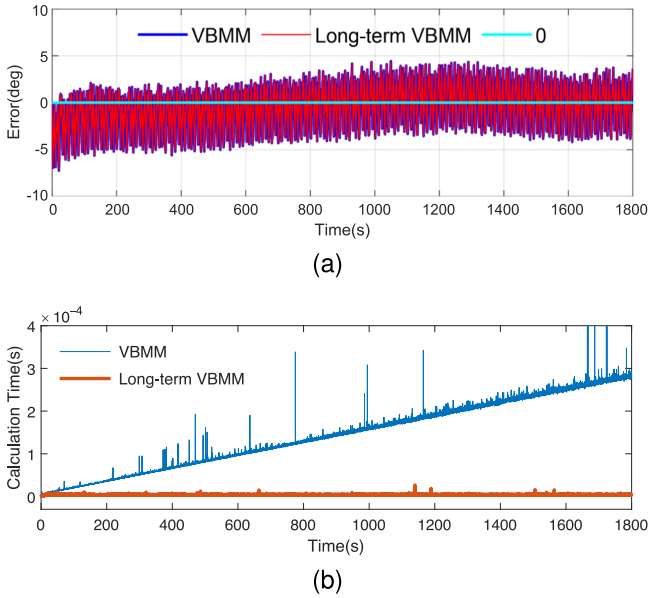

Fig. 17. Results of the long-term experiment (1800 s, VBMM vs. long-term VBMM). (a) Time-error graph. (b) Time-calculation time graph.

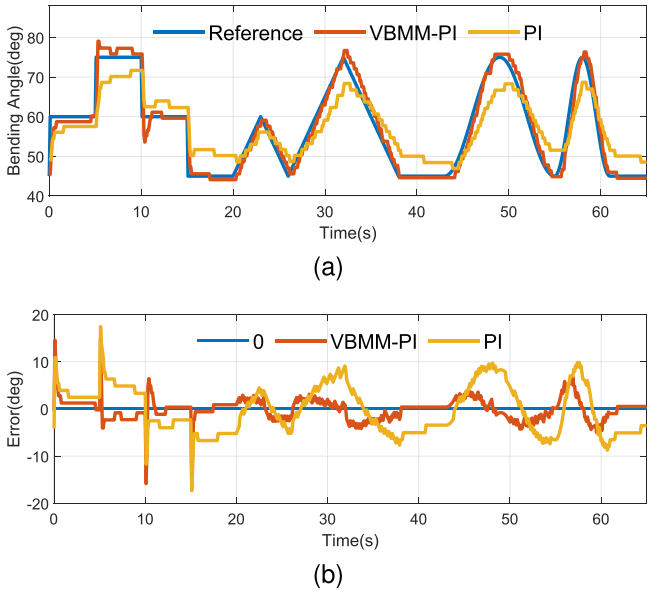

Fig. 18. Results of the control experiment (PI vs. VBMM-PI). (a) Time-angle graph. (b) Time-error graph.

C. *Experiment 2: Validation of the Effectiveness of the Long-Term Model Prediction Mechanism*

To validate the effectiveness of the long-term model prediction mechanism, we conducted a 1800 s test (60 repeated cycles of the variable amplitude experiment). The error curves for VBMM and long-term VBMM coincide exactly (Fig. 17(a)). Both VBMM and long-term VBMM achieved identical accuracy (RMSE=2.148°). There is no difference in accuracy on the order of 10^{-3}. However, while VBMM's computation time grew linearly, the long-term VBMM maintained about 4 μs (97% reduction, Fig. 17(b)). This demonstrates its real-time control capability without sacrificing precision.

D. Experiment 3: Control Performance

To validate the control performance of the feedforward-feedback hybrid control system (simplified as VBMM-PI), we designed challenging reference signals including step signals (45°-75° in 15° increments), variable amplitude sawtooth signals (15°/30°) and variable frequency sinusoidal signals (0.042/0.083 Hz), as shown in Fig. 18(a). Using identical PI gains (P=0.04, I=0.01), VBMM-PI reduced RMSE by 52.9% (2.411° vs. 5.116°) versus baseline PI, maintaining consistent tracking across all signal types (Fig. 18(b)). Experiment 3 demonstrates that using the long-term VBMM as a feedforward significantly improves the control performance of the PI controller, while laterally reflecting the high precision of VBMM.

VI. Conclusion

This paper proposes a viscoelasticity-based mechanistic model and a feedforward-feedback hybrid control system for bending pneumatic muscles. The VBMM combined with the viscoelastic constitutive relations explains the hysteresis and creep properties of BPMs from a mechanistic point of view. Further, we propose a long-term model prediction mechanism based on a sliding window, which reduces the computational burden while maintaining accuracy. Leveraging this model, we develop a feedforward-feedback hybrid control system. Several experiments are performed, including the variable amplitude experiment, the variable loading rate experiment, the long-term experiment, and the control experiment. These experiments demonstrate that VBMM is capable of predicting the strong hysteresis and creep properties of BPMs with high accuracy, and that the feedforward-feedback hybrid control system using the long-term VBMM as the feedforward achieves BPM motion tracking. Our future work will focus on the application of BPMs in the field of rehabilitation.

References

[1] Q. Guan, J. Sun, Y. Liu, N. M. Wereley, and J. Leng, "Characterization and nonlinear models of bending extensile/contractile pneumatic artificial muscles," *Smart Mater. Struct.*, vol. 30, no. 2, 2021, Art. no. 025024.

[2] D. Bruder, X. Fu, R. B. Gillespie, C. D. Remy, and R. Vasudevan, "Data-driven control of soft robots using koopman operator theory," *IEEE Trans. Robot.*, vol. 37, no. 3, pp. 948–961, Jun. 2021.

[3] M. Irshaidat, M. Soufian, A. Al-Ibadi, and S. Nefti-Meziani, "A novel elbow pneumatic muscle actuator for exoskeleton arm in post-stroke rehabilitation," in *Proc. 2nd IEEE Int. Conf. Soft Robot.*, New York, USA, 2019, pp. 630–635.

[4] T. Vo-Minh, T. Tjahjowidodo, H. Ramon, and H. V. Brussel, "A new approach to modeling hysteresis in a pneumatic artificial muscle using the Maxwell-slip model," *IEEE-ASME Trans. Mechatron.*, vol. 16, no. 1, pp. 177–186, Feb. 2011.

[5] T. V. Minh, B. Kamers, H. Ramon, and H. V. Brussel, "Modeling and control of a pneumatic artificial muscle manipulator joint–part : Modeling of a pneumatic artificial muscle manipulator joint with accounting for creep effect," *Mechatronics*, vol. 22, no. 7, pp. 923–933, 2012.

[6] T. Cui et al., "Hysteresis characteristics of pneumatic artificial muscle," in *Proc. 8th Int. Conf. Robot., Control Autom.*, Shanghai, China, 2024, pp. 334–337.

[7] M.-D. Duong, Q.-T. Pham, T.-C. Vu, N.-T. Bui, and Q.-T. Dao, "Adaptive fuzzy sliding mode control of an actuator powered by two opposing pneumatic artificial muscles," *Sci Rep*, vol. 13, no. 1, 2023, Art. no. 8242.

[8] X. Zhang, N. Sun, G. Liu, T. Yang, and J. Yang, "Disturbance preview-based output feedback predictive control for pneumatic artificial muscle robot systems with hysteresis compensation," *IEEE-ASME Trans. Mechatron.*, vol. 29, no. 5, pp. 3936–3948, Oct. 2024.

[9] J. Wang et al., "Model-based linear control of nonlinear pneumatic soft bending actuators," *Smart Mater. Struct.*, vol. 33, no. 4, 2024, Art. no. 045022.

[10] J. Wang et al., "An improved koopman-mpc framework for data-driven modeling and control of soft actuators," *IEEE Robot. Autom. Lett.*, vol. 8, no. 2, pp. 616–623, Feb. 2023.

[11] J. Wang, B. Xu, J. Liu, Z. Zhao, W. Peng, and A. Song, "Robust koopman-mpc approach with high-order disturbance observer for control of pneumatic soft bending actuators under external loads," *IEEE-ASME Trans. Mechatron.*, early access, Jan. 13, 2025, doi: 10.1109/TMECH.2024.3521888.

[12] S. Wang, R. Wang, J. Yang, and L. Hao, "Online incremental dynamic modeling using physics-informed long short-term memory networks for the pneumatic artificial muscle," *IEEE Robot. Autom. Lett.*, vol. 9, no. 10, pp. 8435–8442, Oct. 2024.

[13] H. Zhang, J. Fan, Y. Qin, M. Tian, and J. Han, "Active neural network control for a wearable upper limb rehabilitation exoskeleton robot driven by pneumatic artificial muscles," *IEEE Trans. Neural Syst. Rehabil. Eng.*, vol. 32, pp. 2589–2597, 2024.

[14] Q. Guan, J. Sun, Y. Liu, N. M. Wereley, and J. Leng, "Novel bending and helical extensile/contractile pneumatic artificial muscles inspired by elephant trunk," *Soft Robot.*, vol. 7, no. 5, pp. 597–614, 2020.

[15] H. Al-Fahaam, S. Davis, and S. Nefti-Meziani, "The design and mathematical modelling of novel extensor bending pneumatic artificial muscles (ebpams) for soft exoskeletons," *Robot. Auton. Syst.*, vol. 99, pp. 63–74, 2018.

[16] X. Liu, J. Zhang, S. Gu, L. Zhao, and Z. Li, "Modelling and angle tracking control for multi-chamber soft bending pneumatic muscle," *IEEE Robot. Autom. Lett.*, vol. 8, no. 11, pp. 7647–7654, Nov. 2023.

[17] G. Wang, N. M. Wereley, and T. Pillsbury, "Non-linear quasi-static model of pneumatic artificial muscle actuators," *J. Intell. Mater. Syst. Struct.*, vol. 26, no. 5, pp. 541–553, 2015.

[18] S. Zabihollah, S. A. Moezi, and R. Sedaghati, "Development of enhanced force models to analyze the nonlinear hysteresis response of miniaturized pneumatic artificial muscles," *Smart Mater. Struct.*, vol. 33, no. 8, 2024, Art. no. 085043.

[19] N. G. McCrum, C. P. Buckley, and C. B. Bucknall, *Principles of Polymer Engineering*. Oxford, U.K.: Oxford Univ. Press, 1997.

[20] W. N. Findley and F. A. Davis, *Creep and Relaxation of Nonlinear Viscoelastic Materials*. North Chelmsford, MA, USA: Courier Corporation, 2013.

[21] S. Reese and S. Govindjee, "A theory of finite viscoelasticity and numerical aspects," *Int. J. Solids Struct.*, vol. 35, no. 26, pp. 3455–3482, 1998.

[22] J. S. Bergström and M. C. Boyce, "Large strain time-dependent behavior of filled elastomers," *Mech. Mater.*, vol. 32, no. 11, pp. 627–644, 2000.

[23] R. L. Bagley and P. J. Torvik, "On the fractional calculus model of viscoelastic behavior," *J. Rheol.*, vol. 30, no. 1, pp. 133–155, 1986.

[24] G. Andrikopoulos, G. Nikolakopoulos, and S. Manesis, "An experimental study on thermodynamic properties of pneumatic artificial muscles," in *Proc. 20th Mediterr. Conf. Control Autom.*, Barcelona, Spain, 2012, pp. 1334–1340.

[25] B. Tondu, "Modelling of the mckibben artificial muscle: A review," *J. Intell. Mater. Syst. Struct.*, vol. 23, no. 3, pp. 225–253, 2012.

[26] A. P. Boresi and R. J. Schmidt, *Advanced Mechanics of Materials*. Hoboken, NJ, USA: Wiley, 2002.